Experimental Measurements of the Dispersion and Growth Rate of Ion Acoustic Waves in the Plume of a Hollow Cathode

IEPC-2024-366

Presented at the 38th International Electric Propulsion Conference, Toulouse, France
June 23-28, 2024

Miron F. Liu* and Benjamin A. Jorns†
University of Michigan, Plasmadynamics and Electric Propulsion Laboratory, Ann Arbor, MI, 48109

Experimental measurements of the dispersion and frequency-resolved growth rate of ion-acoustic waves in a krypton hollow cathode plume are obtained using a bispectral analysis technique based on two-probe correlation. The dispersion measured using this method was found to be in agreement with the results of Beall analysis and the predictions from linear theory. The measured growth rates also appear to be commensurate with theoretical predictions and suggests damping of waves from ion-neutral collisions at low frequencies. The electron Mach number range of 0.27 - 0.55 inferred from these measurements are consistent with experimentally measured values for similarly configured cathodes. Minor undulations in the growth rate plot are observed and attributed to the presence of ionization instabilities in the hollow cathode plume, and/or to nonlinear cross-length scale coupling of wave energy which are not measured in this work. In light of these results, for the frequency range and operating condition of this work, the theoretical linear scaling of ion acoustic wave growth rates with frequency appears to be an appropriate assumption for hollow cathode modeling.

I. Introduction

Hollow cathodes are commonly employed as both neutralizers and plasma sources for various plasma electric propulsion (EP) systems. In these devices, gradients in electric potential established to facilitate electron extraction also give rise to the growth of plasma instabilities. Ion-acoustic waves, in particular, have been identified as a dominant mode in the plume of hollow cathodes [1][2] where the growth and saturation of these waves into ion-acoustic turbulence (IAT) has been linked to non-classical resistivity for electrons [3]–[5] and anomalous heating of ions [6]–[14]. Given that these effects can significantly influence electron and ion dynamics in the discharge, it is necessary to account for them in the modeling of hollow cathodes. However, despite concerted efforts to incorporate these wave-driven effects in numeric codes [4][5], the direct relationship between wave properties, anomalous electron resistivity, and ion heating remains poorly understood. This has precluded the development of self-consistent predictive models.

In light of this knowledge gap, there has been a series of experimental and numerical work to relate the onset of plasma instabilities to non-classical transport processes in hollow cathodes. Most experimental and computational efforts have employed quasilinear theory to translate measurements of key wave properties to enhanced electron resistivity and ion heating[1][15][16]. While these efforts have aided in the explanation of key trends observed in the plasma state, there remain open questions about the validity of the theoretical frameworks employed to assess the role of the instabilities in driving anomalous transport. For example, recently it has been suggested that, for other electrostatic instabilities in EP-based low-temperature plasmas, a quasilinear formulation for growth rate may not be entirely appropriate [17].

To achieve a comprehensive understanding of how IAT drives anomalous particle and energy transport, the need is thus apparent to develop experimental methodologies to directly measure the growth rates of

*PhD Pre-candidate, Aerospace Engineering, mironliu@umich.edu
†Associate Professor, Aerospace Engineering, bjorns@umich.edu

these waves. Previous efforts have attempted to infer these growth rates indirectly. Most recently, for example, Jorns et al. measured the average growth rate of IAT in a hollow cathode by evaluating the change in the total wave energy density over a finite distance [15]. While this effort did serve to confirm that, on average, the growth rate could be explained by linear theory, the method employed did not have resolution in frequency space, i.e. the growth was not resolved for different frequency components of the spectrum. To our knowledge, there have been no frequency-resolved measurements of the growth rate of IAT in a hollow cathode plume to date. Obtaining this data will allow for more detailed estimates of the dynamics governing IAT propagation and, by extension, their influence on the transport properties of the cathode plume [18]. The goal of this work is to provide direct experimental measurements of both the dispersion and frequency-resolved growth rate of ion-acoustic waves in a hollow cathode plume based on a novel spectral analysis technique recently demonstrated by Brown and Jorns[17].

With this purpose in mind, this paper is structured as follows. In section II we detail the theoretical framework used to relate anomalous transport to wave properties of ion-acoustic waves. In section III we provide a review of the analysis techniques employed in this work. In section IV we describe our experimental apparatus used to resolve key wave properties of IAT in the plume of a hollow cathode. We then present our results in section V followed by a discussion of our findings in section VI. Finally, in section VII we present a summary of the work and key conclusions drawn.

II. Theory of Ion Acoustic Waves

The ion acoustic instability is an electrostatic wave mode that can spontaneously onset in plasma exhibiting large disparities in ion and electron temperatures and drift velocities [19]–[21]. These two conditions are met in the plume of hollow cathodes, and recent experimental efforts have confirmed the existence of such waves in these devices [1][2]. The theoretical framework for characterizing the presence and behavior of waves in plasma is the dispersion relation. The dispersion relation for ion-acoustic waves in the hollow cathode plasma can be derived from the Boltzmann equations for ions and electrons through linear analysis [1][22] subject to the simplifying assumptions characteristic to plasma parameters in a hollow cathode plasma: $|\vec{v_i}| \ll c_s \ll |\vec{v_e}| \ll v_{th_e}$, where $c_s = \sqrt{\frac{qT_e}{m_i}}$ is the ion sound speed, $v_{th_e} = \sqrt{\frac{qT_e}{m_e}}$ is the electron thermal speed, $\vec{v_i}$ is the ion drift velocity, $\vec{v_e}$ is the electron drift velocity. Here q, T_e, m_i, and m_e denote elementary charge, electron temperature, ion mass, and electron mass, respectively. The real part of the dispersion relation is given by [22]

$$\omega_{RE} = \frac{kc_s}{\sqrt{1+k^2\lambda_{De}^2}} + \vec{k}\cdot\vec{v_i}, \tag{1}$$

where ω_{RE} denotes the real component of angular frequency, $\lambda_{De} = (\frac{\varepsilon_o T_e}{n_e q^2})^{1/2}$ is the electron Debye length, k is the wavenumber (spatial frequency of a wave mode), and $\vec{k}$ is the wave vector. Here ε_o and n_e denote the permittivity of free space and electron number density. Noting that the experimentally observed frequencies at which ion-acoustic waves have been found to propagate at are lower than the ion plasma frequency [1], $\omega_{RE} \ll \omega_{pi}$, and at low wavenumbers, we may approximate Eq. 1 in the limit $\lambda_{De}k \ll 1$ as (c.f. [22])

$$\omega_{RE} = kc_s + \vec{k}\cdot\vec{v_i}. \tag{2}$$

By inspection of the first term on the right-hand side, it is evident that in the reference frame of the ions, these waves propagate at the ion-sound speed, whence they derive their name. The second term on the right-hand side of Eq. 2 represents a Doppler shift, i.e. a transformation of the wave speed from the ion frame into the lab frame.

Per [22] the imaginary part of the dispersion relation, ω_{IM}, i.e. the linear theoretical growth rate, is given by

$$\omega_{IM} = \gamma = \left(\frac{\pi}{8}\right)^{\frac{1}{2}} c_s k \left[\frac{\vec{k}\cdot(\vec{v_e}-\vec{v_i}) - kc_s}{kv_{th_e}} - \left(\frac{T_e}{T_i}\right)^{\frac{3}{2}} e^{-\frac{T_e}{2T_i}}\right] - \frac{\nu_{in}}{2}. \tag{3}$$

Here T_e and T_i are electron and ion temperatures and ν_{in} is the ion-neutral collision frequency. Physically, the first term on the right-hand side of this equation represents the growth of the wave from inverse Landau damping of the electron species. The second term encodes damping of the wave from ion Landau damping. The last term captures the damping of the wave due to classical ion-neutral collisions. For the plasma

conditions typical of the cathode plume, the magnitudes of the ion sound speed and ion drift can be neglected with respect to the electron drift. Similarly, the ion Landau damping term can be neglected compared to the ion collisional term for $T_e >> T_i$ which is valid for cathode plasma [1]. Lastly, we note that the wave growth is dominant in the direction of electron drift, i.e. along the center line of the cathode. For this being the case, we may thus eliminate vector notation and recast Eq. 3 in terms of scalar quantities as

$$\omega_{IM} = \gamma = \left(\frac{\pi}{8}\right)^{\frac{1}{2}} c_s k M_e - \frac{\nu_i}{2}. \tag{4}$$

Here M_e denotes electron Mach number. Equations 2 and 4 define the ion acoustic dispersion relation used in our analysis.

III. Analysis methods for inferring wave properties

We detail in this section two methods for inferring the properties of the ion-acoustic wave propagation. The first is a histogram-like analysis method developed by Beall et al. which yields a statistical description of wave dispersion through binning of wavenumber-frequency pairs [23]. The second "bispectral analysis" method involves solving a wave equation for parameters encoding both the dispersion and growth rate of propagating wave modes.

A. Beall analysis

The Beall method we introduce here is a spectral analysis technique that leverages correlated measurements of plasma potential fluctuations taken at a pair of spatially separated probes. Using this data we may generate a probabilistic distribution of wave dispersion over frequency-wavenumber space. This method has been employed in the context of hollow cathodes in the works of Jorns et al., Cusson et al., Georgin, and Mooney and Lemmer [1][2][24][25]. To illustrate this approach, we show in Fig. 1 a notional schematic of the probe configuration used to resolve spectral properties of propagating ion-acoustic modes in a hollow cathode plume.

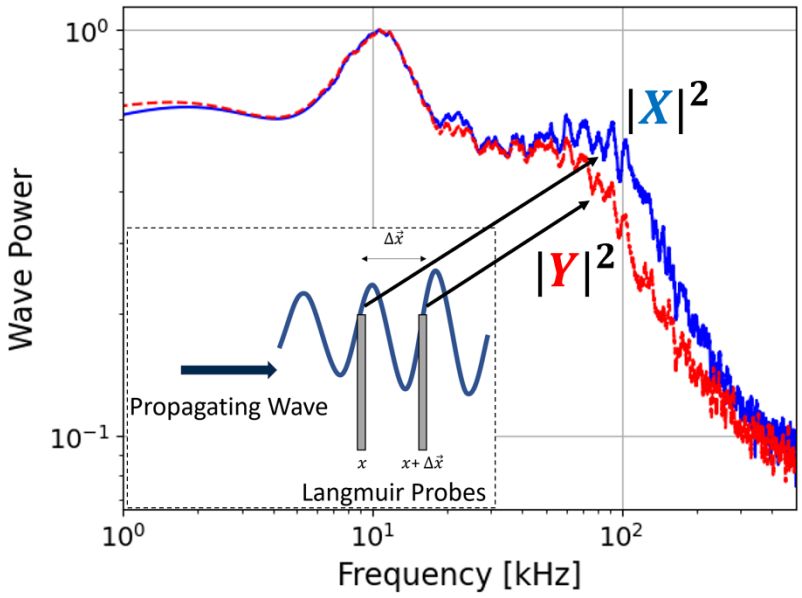

Figure 1: Notional diagram of analysis technique

A pair of ion-saturation probes (lower left in Fig. 1) is inserted into the plasma to monitor time-resolved plasma potential fluctuations induced by propagating waves at two physically separated locations, $\phi(x,t)$ and $\phi(y,t)$ where $y = x + \Delta\vec{x}$. We can then Fourier transform these two signals to find their spectral content, i.e. complex amplitude as a function of frequency, f, denoted X_f for the probe at location x, and Y_f for the probe at location $x + \Delta\vec{x}$. Taking moments of X_f and Y_f allows us to obtain higher-order spectral information such as, for example, the power spectra (shown in red and blue in Fig. 1) and cross-power

spectra. Following the formulation given in [1] we may leverage the aforementioned higher-order spectral information to solve for the wavenumber along the vector connecting the two probe tips where the maximum resolvable wavenumber is dictated by the inter-probe spacing, $|k| < \pi/\Delta\vec{x}$

$$k_x(f) = \frac{1}{\Delta\vec{x}}\tan^{-1}\left[\frac{\mathcal{I}m(Y_f X_f^*)}{\mathcal{R}e(Y_f X_f^*)}\right]. \tag{5}$$

Here "*" denotes complex conjugation. As noted in [1][23], this technique is sensitive to noise and can be errant if there are multiple modes present in the plasma, i.e. multiple wavenumbers per frequency. In light of this, we employ the probabilistic approach proposed by Beall et al. where we first collect M samples of spectra, then evaluate wavenumber as a function of frequency according to Eq. 5 for each sample, and lastly apply a weighted binning of the wavenumber-frequency pairs according to

$$S(f,k) = \frac{1}{M}\sum_{j=1}^{M} I_{0,\Delta k}[k^i - k^j(f)]\frac{1}{2}[P_1^j(f) + P_2^j(f)]. \tag{6}$$

Here S denotes the "intensity", i.e. the weighted number of data points that fall within each bin, j denotes the sample index, i denotes the wavenumber index in the discretized wavenumber domain, P_1 and P_2 are the power spectra of fluctuations measured at x and y, respectively, i.e. XX^* and YY^*, and $I_{0\Delta k}$ is an indicator function governed by

$$I_{0\Delta k} = \begin{cases} 1 & \text{if } |x| < \Delta k \\ 0 & \text{otherwise.} \end{cases} \tag{7}$$

In principle, iterating through every sample j, across every frequency f, and wavenumber i and applying the binning method described by Eqns. 6 and 7 where $\Delta k = k^i - k^j(f)$ we obtain a 2D histogram that yields S as a function of frequency and wavenumber. Larger values of S indicate frequency-wavenumber pairs that are dominant in the measurement domain. Given measurements of wave growth can be obtained, we can apply a similar binning method by replacing $k^i - k^j(f)$ in Eq. 6 with $\gamma^i - \gamma^j(f)$

$$S(f,k) = \frac{1}{M}\sum_{j=1}^{M} I_{0,\Delta k}[\gamma^i - \gamma^j(f)]\frac{1}{2}[P_1^j(f) + P_2^j(f)]. \tag{8}$$

B. Bispectral analysis framework

The bispectral analysis method we detail here is a technique pioneered by Ritz et al., modified by Kim et al., and recently demonstrated by Brown and Jorns on the plume of a Hall effect thruster [17][26]–[28]. While this technique leverages the same two-probe correlation diagnostic as the Beall method, both the dispersion and growth rate of waves may be obtained by relating X_f and Y_f through a wave equation. This relationship can be represented functionally, as detailed by Brown and Jorns [17], through the relation (see Appendix)

$$Y_f = L_f X_f + \sum_{f=f_1+f_2} Q_f^{1,2} X_{f_1} X_{f_2}. \tag{9}$$

Here L_f encodes the dispersion and linear growth rate in the direction defined by the axis connecting the two probes for a wave mode with frequency f. Q_f encodes the non-linear growth from wave-wave coupling. We note there is one L_f parameter for every frequency in the domain and one Q_f parameter for every frequency triple that satisfies $f = f_1 \pm f_2$. Physically, Eq. 9 posits that the spectrum at location x, i.e. X_f, changes through both linear growth processes (L_k) and non-linear wave-wave interactions (Q_k), and thus evolves during its propagation over a finite distance $\Delta\vec{x}$ into the spectrum observed at location $x + \Delta\vec{x}$, i.e. Y_f.

In a departure from Brown and Jorns, in this work, we do not solve for non-linear growth parameters. This is because it has been shown that cross-length scale wave energy coupling occurs most strongly from the MHz frequency regime down into lower frequencies [17]. However, the maximum resolvable frequency in our measurement domain is 500 kHz. Furthermore, as we will show in section VI, the regime of propagation of the IAT waves we measure only extends up to approximately 100 kHz. We thus do not expect strong non-linear energy coupling from frequencies in the upper bound of our measurement domain down to lower frequencies within our measurement domain. We therefore approximate Eq. 9 as

$$Y_f = L_f X_f. \tag{10}$$

We acknowledge that, although we likely cannot resolve strong non-linear wave energy coupling within our measurement domain, wave modes in the MHz regime likely still deposit energy into waves at these lower frequencies [17]. This represents an effective source term that we cannot resolve and is thus a potential source of error. Nevertheless, following the formulation in Ritz et al., applying this simplification allows us to directly solve for the growth rate and wavenumber as functions of frequency through the cross-correlation of probe data [26][27] without the comparatively significant computational overhead associated with additionally solving for non-linear growth parameters

$$\gamma_f = \mathcal{R}e\left(\frac{|\langle Y_f X_f^*\rangle|}{\langle X_f X_f^*\rangle} - 1 + \ln\left(\frac{\langle Y_f X_f^*\rangle}{|\langle Y_f X_f^*|\rangle}\right)\right)\frac{1}{\Delta\vec{x}}\cdot\vec{v}_g, \tag{11}$$

$$k_{f(\Delta\vec{x})} = \mathcal{I}m\left(\frac{|\langle Y_f X_f^*\rangle|}{\langle X_f X_f^*\rangle} - 1 + \ln\left(\frac{\langle Y_f X_f^*\rangle}{|\langle Y_f X_f^*\rangle|}\right)\right)\frac{1}{\Delta\vec{x}}. \tag{12}$$

In the equations above, the bracketed quantities denote ensemble averaging across multiple measurements of the spectra. In Eq. 11 $\vec{v}_g = \frac{\partial\omega_f}{\partial\vec{k}_f}$ denotes the group velocity of the wave, i.e., the velocity at which wave-packets travel. This group velocity can be determined experimentally by first obtaining wavenumber as a function of frequency per Eq. 12. Eqns. 11 and 12 allow us to infer key wave properties from measurements of plasma potential fluctuations. We discuss how these data are obtained in the next section.

IV. Experimental Apparatus

We outline in this section the experimental configuration and methods we employ in our work. We first present the test article and facility. We then overview the diagnostics and analysis techniques.

A. Hollow Cathode Test Article

The test article shown in Fig. 2 is a lanthanum hexaboride (LaB_6) hollow cathode designed for the 9-kW H9 Hall thruster with a nominal operating current of 15-20 A [29][30]. We operate the cathode on krypton at a 6.2 A, 20-sccm condition in our test. We place a water-cooled cylindrical anode downstream of the cathode to sustain discharge. To allow the cathode and anode to settle to thermal steady state, and the chamber to pressure steady state, we operate the cathode for an hour at the above conditions prior to data collection. The cathode-anode voltage as reported by the power supply at the end of this period was 44 V.

B. Facility

We test the H9 cathode in the Cathode Test Facility (CTF). This 0.6 m in diameter by 1 m long vacuum facility (Fig. 3) is pumped by a 135 CFM mechanical roughing pump and a 20" CVI TM500 cryopump with a measured pumping speed of 1500 L/s on Xe. The chamber can achieve a typical base pressure of 1×10^{-6} Torr-N_2. An InstruTech IGM401 Hornet ion gauge is employed to monitor chamber pressure.

Figure 2: H9 LaB_6 hollow cathode

Figure 3: Cathode test facility (CTF)

C. Wave Probes

In principle, for low-amplitude electrostatic waves, ion saturation current fluctuations can be used as a proxy for the plasma potential fluctuations associated with propagating waves [1][2][31]. Assuming electron temperature fluctuations are slow on the timescale of the wave propagation, we can express this relationship as

$$\tilde{\phi}(t) = \frac{T_e}{q}\frac{\tilde{I}_{sat}}{\bar{I}_{DC}}, \tag{13}$$

where $\tilde{I}_{sat}$ denotes the time-varying component of the ion saturation current and $\bar{I}_{DC}$ is the time-averaged component. To measure such fluctuations in plasma, we employ a pair of Langmuir probes biased -37V to ion-saturation mode using batteries. The cylindrical tungsten probe tips measure 0.5 mm in diameter and 5 mm in length for a total collection area of 8.05 mm^2. The anode is placed 55 mm downstream of the cathode keeper orifice. The central probe is placed 25 mm from the cathode keeper orifice with an inter-probe spacing of 4 mm. The test configuration and corresponding schematic are shown in Figs. 4 and 5.

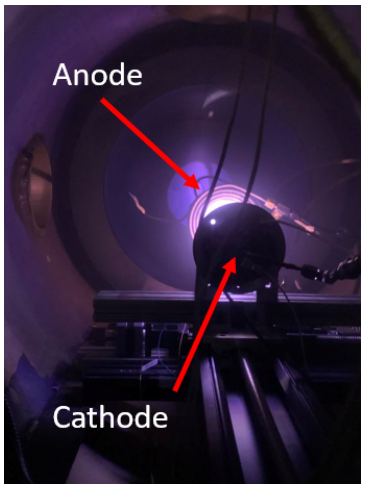

Figure 4: Testing configuration

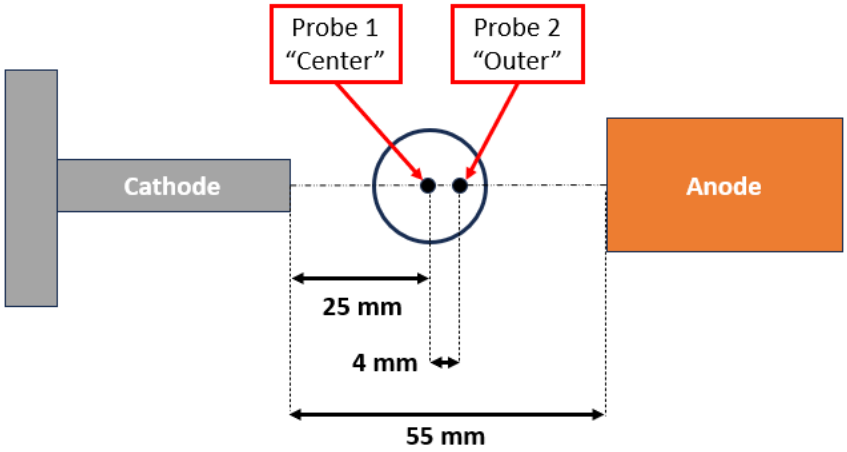

Figure 5: Experimental arrangement schematic

Time-resolved ion-saturation current fluctuations are inferred by measuring the voltage drop across a 100-Ω low-inductance metal foil resistor using a Keysight DSO-X 3024 Oscilloscope. We show the current sensing circuit diagram in Fig.6.

The oscilloscope is configured to sample at a temporal resolution of 1 μs corresponding to a maximum Nyquist frequency of 500 kHz. The measured bandwidth of the current sensing circuit is 3.4 MHz which exceeds the upper bound of the frequency domain relevant to this study. We thus ensure that our collected data is unaffected by signal attenuation. We acquire 100 ion saturation current traces, each spanning 2 ms. Each trace is subsequently divided into 10 intervals, resulting in a total of 1000 samples. We then Fourier transform these samples to yield 1000 spectral pairs with frequency resolutions of 500 Hz. To reduce stochastic noise, we ensemble average across all samples when computing the auto-power and cross-power spectra per Eqns. 11 and 12. For consistency, we use the same dataset for the Beall analysis.

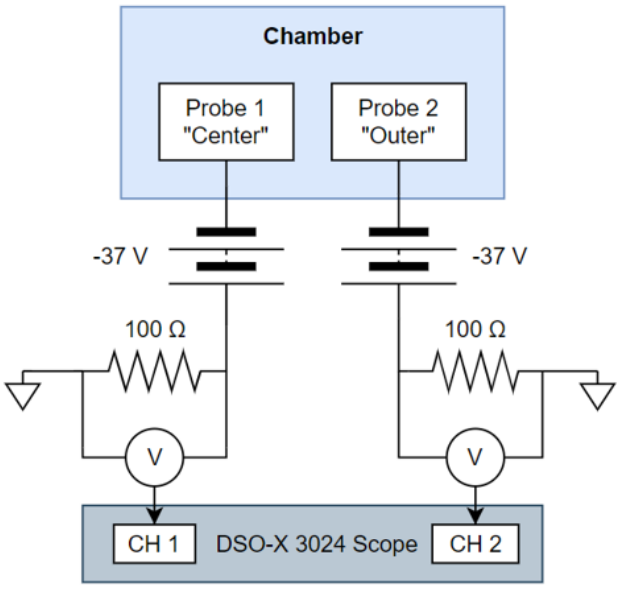

Figure 6: Current sensing circuit diagram

V. Results

We present in this section results for the single cathode operating condition described in the preceding. We first show results for the power spectrum of the two waves. We then present results for the inferred dispersion. We conclude with estimates for the experimentally measured growth rates.

A. Power spectra

We first show in Fig. 7 power spectra from the two probe positions averaged over 100 ensembles (full-length traces) and then smoothed using 5^{th}-order Savitzky-Golay filtering with a window size of 250. There are a few features here consistent with previous experimental reportings of these devices. We first note a maximum in wave power near 40 kHz followed by an inverse power law decay at higher frequencies commensurate with turbulent spectra [19] and previous observations [1][24][25]. We also observe undulations in the spectra at lower frequencies characterized by local peaks in spectra starting at around 10 kHz with harmonics extending until the regime of inverse power law decay. While these peaks are less prominent compared to previous work, this feature is consistent with ionization instability-induced multi-peaked spectra studied extensively by Georgin [24].

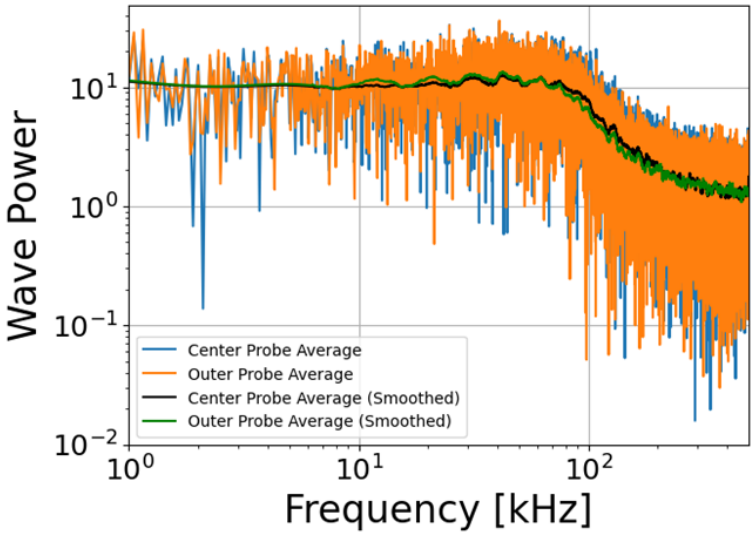

Figure 7: Averaged and smoothed power spectra

B. Dispersion

We next show in Fig. 8 a plot of the wave dispersion resolved through bispectral analysis per Eq. 11 overlaying a Beall intensity plot. The "intensity" shown on the third axis is the number of data points that fall into each frequency-wavenumber bin. To aid in visualization we plot the natural log of intensity. We note that the same set of 1000 ion-saturation current traces is used for both techniques and results in a shared frequency resolution of 500 Hz. The wavenumber resolution for the Beall analysis is set to 0.785 m^{-1} such that both axes achieve the same degree of discretization (i.e. the histogram has square bins).

For a more direct comparison with the results of the Beall analysis, we applied a Beall-like analysis to the wavenumbers obtained from bispectral analysis by substituting Eq. 12 without ensemble averaging, in lieu of Eq. 5 for wavenumber, into Eq. 6. This allows us to bin the wavenumbers and generate a Beall plot-like histogram which we can compare directly with a Beall intensity plot. We show the this result in Fig. 9

There are three notable features that emerge from the analysis of both methods. We first note that the most probable values obtained from the Beall technique and the ensemble-averaged values (red) obtained from bispectral analysis are coincident. This is unsurprising as the Beall intensity plot yields the effective "mode" of dispersion while the bispectral method, which employs ensemble averaging, reflects the "mean" dispersion. Given sufficient number of samples to reduce the impact of noise-induced outliers we expect these two values to be similar. A comparison of the Beall plot (Fig. 8) and the Beall plot-like histogram (Fig. 9) generated using wavenumbers obtained from the bispectral analysis without ensemble averaging shows strong agreement between the techniques.

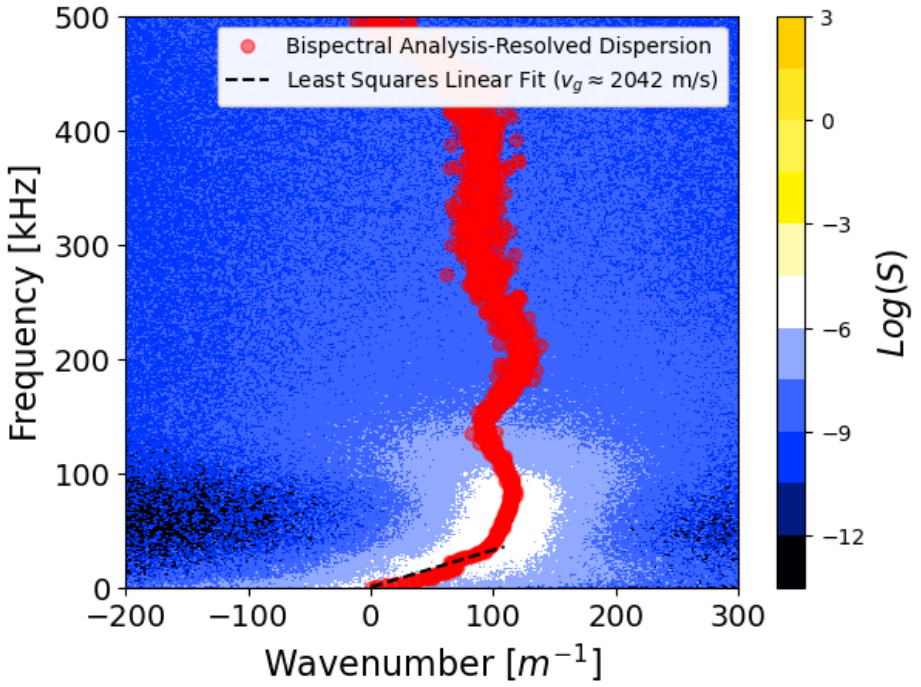

Figure 8: Bispectral analysis-resolved dispersion overlayed on Beall Plot

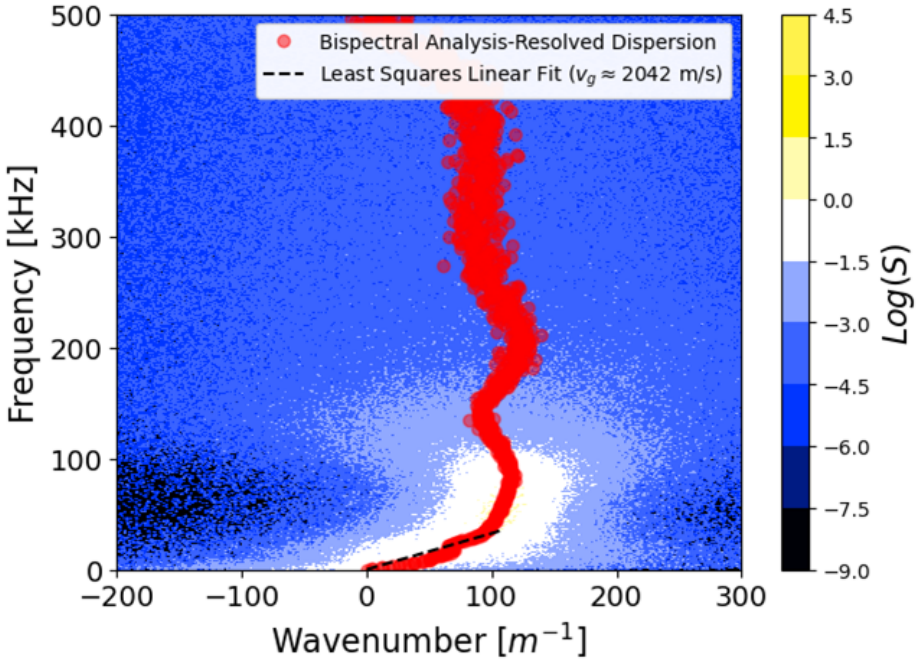

Figure 9: Bispectral analysis-resolved dispersion overlayed on Beall plot-like histogram generated from non-ensemble averaged bispectral analysis-resolved wavenumbers

The second notable feature is that the dispersion is approximately linear over the frequency range of 0 to 40 kHz for both techniques. This is broadly consistent with previous studies using the same class of cathode [2][24] and indicates the presence of low-frequency propagating ion-acoustic waves. To this point, we note the best-fit slope of this line suggests a group velocity of approximately 2041 m/s. In light of our linear dispersion relationship and assuming zero ion drift velocity, this could be explained by an electron temperature of approximately 3.6 eV. This would be consistent with, though on the higher end of, measured temperatures in these devices. Lower temperatures could result if we account for finite ion drift. For example, if we allow for an ion drift velocity of 1 km/s – on the order of experimentally measured ion drift velocities in a cathode plume [15] – the corresponding electron temperature would fall to approximately 1 eV.

The final feature we note is that the wave dispersion disappears above 40 kHz. This suggests that, with the present configuration, the waves either do not propagate above this frequency or are not experimentally resolvable. This contrasts with previous findings which observed that the ion acoustic waves persisted to frequencies exceeding 2 MHz [1]. However, this discrepancy can potentially be explained by the drastically differing operating conditions between these studies.

C. Growth rate

As a final result in this section, we show in Fig. 10 a plot of the growth rates resolved through bispectral analysis per Eq. 11 overlaying the corresponding histogram generated using a modified binning algorithm given by Eq. 10. The Beall plot-like histogram has a frequency resolution of 500 Hz and a growth rate resolution of 1 kHz such that the histogram has square bins. Given that the waves only appear to exhibit acoustic-like dispersion up to 40 kHz, we plot in Fig. 11 the growth rates over this frequency range. Additionally, we include a best-fit line and indicate the y-intercept and slope.

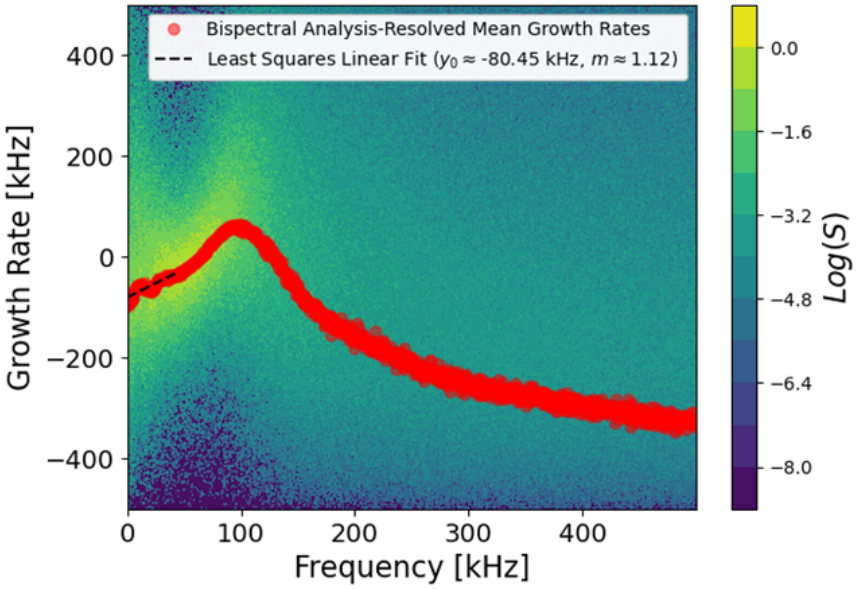

Figure 10: Bispectral analysis-resolved growth rate overlayed on Beall plot-like histogram

Three key features emerge from this result. First, the negative growth rates suggest damping of the waves over this frequency range. Secondly, aside from minor undulations, the growth rate demonstrates an approximately linear relationship across the frequency range. This is consistent with Eq. 11 which predicts a linear dependence of growth rate on frequency. By fitting a line to this result we can infer the electron Mach number given other parameters per equation 11. The slope of this line encodes the electron Mach number, which is a function of electron temperature, and the y-intercept encodes the ion-neutral damping rate. Assuming an electron temperature range of 1 - 3 eV we may estimate an electron Mach number range of approximately 0.27 - 0.55. This is consistent with recent experimental measurements of electron Mach numbers between 0.3 and 0.8 observed in a similar hollow cathode [32]. The third feature is the y-intercept of -80.45 kHz. Per Eq. 11, this offset may suggest an ion-neutral collision frequency of approximately 128 kHz. Given past work on comparably configured cathodes, and in light of the experimentally measured

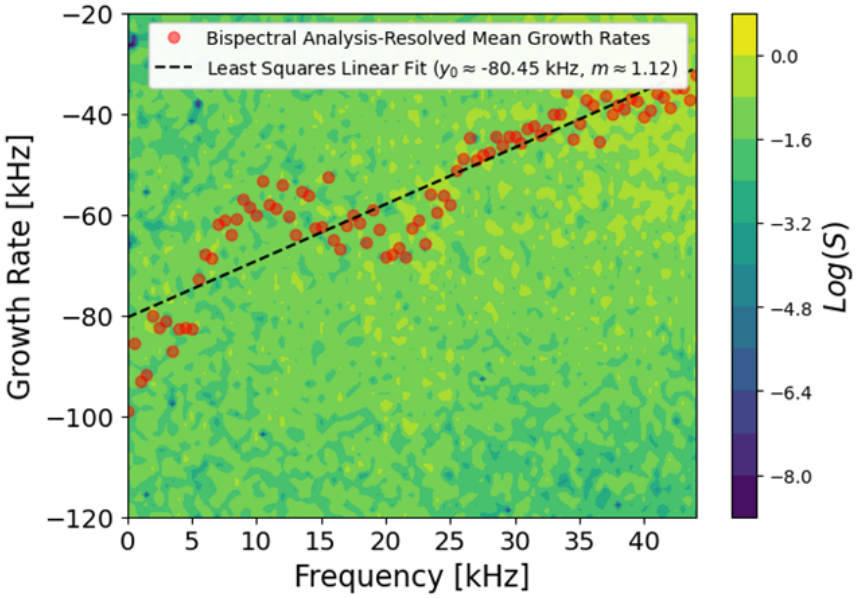

Figure 11: Bispectral analysis-resolved growth rate vs. frequency

charge-exchange cross-section of krypton, this is a physically plausible value [22][33].

Taken together, these results suggest that a linear theoretical growth rate is a reasonable approximation over this range of frequencies, characterized by a positive contribution to wave growth from electron momentum extraction but damping through neutral collisions. This type of damping at low frequencies has previously been discussed as a mechanism for preventing wave propagation at low frequencies and a mechanism for saturation via inverse energy cascades [1][2]. We return to this point in the discussion.

In summary, in this section, we first highlighted key features of the power spectra commensurate with spectra of IAT. We then compared the Beall analysis with bispectral analysis dispersion and found strong agreement between the two methods and with linear theory. Lastly, we presented the first experimentally measured growth rate of ion-acoustic waves which we found also closely aligned with theoretical predictions.

VI. Discussion

In this section, we discuss the results presented above in the context of phenomena that may influence our conclusions. We first discuss the effect of probe shielding and related error. We then detail the impact of ionization waves on our results. We conclude with a discussion of impact of non-linear wave effects and the relationship of our results to wave saturation.

A. Possible influence of probe shielding and related error

We acknowledge that the insertion of physical probes into the plasma is inherently perturbative. In particular, given the positioning of probes in this work along the cathode centerline, the center probe may shield the outer probe from the plume to some extent. Indeed, a comparison of the probe tip elements post-testing supports this hypothesis. It is evident from Fig. 12 that the ceramic sealant on the center probe tip has experienced significantly more erosion compared to the outer probe. It is thus plausible that this shielding may artificially reduce the wave power measured at the outer probe. This would result in measured growth rates which are artificially low and may lead to the spurious conclusion that the waves are being damped. This issue may potentially be mitigated in the future with smaller probe elements or by employing a non-intrusive optical technique.

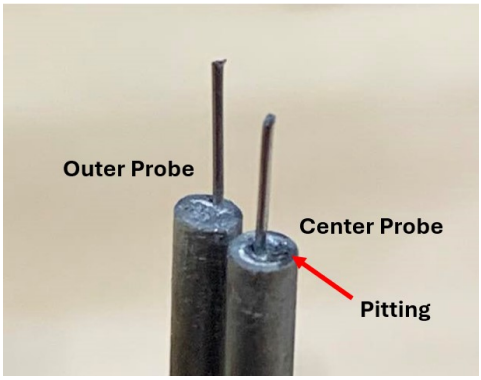

Figure 12: Comparison of probe erosion

B. Impact of ionization waves effects

Next, we note that, although predominantly linear, there are a few non-linear regions in the growth rate vs frequency plot. These undulations coincide with local peaks observed in the power spectra (Fig. 13 and 14).

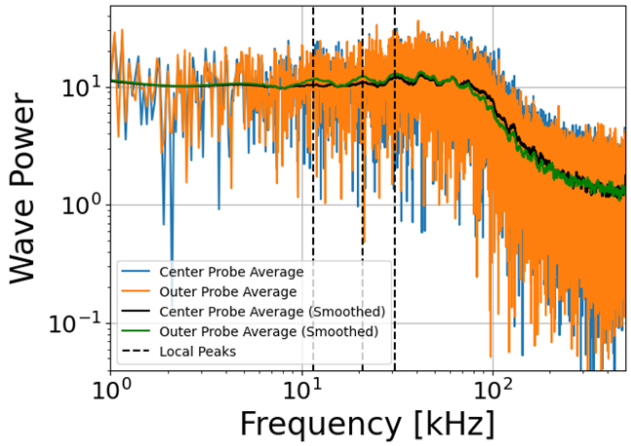

Figure 13: Local peaks in power spectra

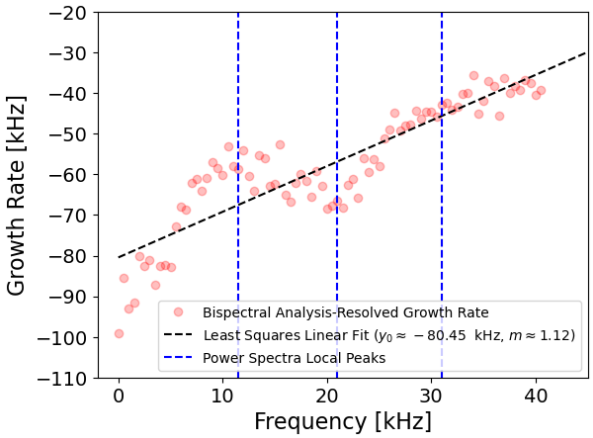

Figure 14: Regions of non-linearity in growth rate

The ionization instability studied extensively by Georgin manifests a multi-peaked power spectrum [24]. It is thus plausible these peaks can be attributed to weak ionization modes. Recent work by Mikellides et al. to characterize hollow cathode dynamics in the 0-500 kHz frequency regime show similar, multi-peaked power spectra from both experiment and simulation [34]. We note that Goebel et al. and Jorns et al. attribute peaks in power spectra in this low-frequency regime to a cathode ionization instability in their work as well, albeit with different cathode operating conditions than in our work [10][15]. It is also possible that non-linear wave-wave coupling contributes to the local non-linearity in the growth rate plot, which we discuss in the following.

C. Impact of non-linear wave effects and relationship of results to wave saturation

A key feature that previously has been pointed out in the context of ion acoustic wave turbulence [19] is that the spectra are often characterized by a global peak followed by an inverse power law decay at higher frequencies [1][2][24]. Simulations have suggested that the inverse power law decay may be the result of non-linear wave coupling effects such as non-linear inverse Landau damping [16], which leads to an effective energy transfer from high-frequency, short length-scales to low-frequency, long length-scales. This transfer of energy is ultimately dissipated at longer length scales by effects such as inter-particle collisions. Our experimental results may be validation of this later process where the negative growth rates broadly indicate a uniform, frequency-independent mechanism at play. This provides a clue for how at least one element of the processes that drive saturation in these devices may be governed.

We note, however, that we cannot directly verify this in this work as we do not measure non-linear contributions to growth in our work. In fact, the neglect of these terms potentially introduces a source of error as waves propagating at frequencies much higher than our maximum resolvable frequency may still deposit energy to waves within our measurable frequency domain. To this point, using a similar bispectral analysis technique, Brown and Jorns found significant non-linear power transfer from waves within the 5-10 MHz regime down to waves in the 200 - 500 kHz regime, albeit within the plume of a Hall effect thruster [17]. Future efforts will need to focus on the non-linear effects to confirm that cross-length scale coupling of wave energy within a hollow cathode plume is indeed occurring within the frequency range and at the operating conditions of this work.

D. Implication of results for hollow cathode modeling

Our findings indicate that, at the low-frequency range and under the specific operating conditions of this work, experimentally measured growth rates are largely consistent with quasilinear theory. This suggests

that nonlinear or kinetic effects altering the distribution function (i.e., quasilinear diffusion) are not significant. This result could inform future models, suggesting that ion acoustic wave growth rates can indeed be treated as linear, at least within the low-frequency ranges and operating conditions explored in this study. However, this conclusion may vary with different operating conditions and spatial locations within the hollow cathode plume. Therefore, future work should focus on parametric studies in addition to spatially resolved measurements of growth rates.

VII. Conclusion

In this work, we applied a bispectral analysis technique to obtain the first frequency-resolved experimental measurements of ion acoustic wave growth rates in a krypton hollow cathode plume at a single operating condition. This method also provided experimental measurement of the wave dispersion which showed strong agreement with the Beall analysis using the same set of data, thereby validating our approach. Furthermore, the best-fit lines derived from experimentally resolved dispersion and growth rates suggest a range of electron temperature, ion drift velocity, and electron Mach number values that align with experimentally measured values in hollow cathode discharge. Our analysis revealed a predominantly linear growth rate, with minor deviations which we attribute to ionization instabilities and/or to non-linear wave-wave coupling effects which we do not measure in this work. Our findings suggest that, for the frequency range and cathode operating condition tested in this work, a quasilinear formulation for growth rate may be an appropriate assumption for hollow cathode numerical codes.

VIII. Acknowledgements

This work is funded by the U.S. Department of Energy, Office of Science, Office of Fusion Energy Sciences, under the Early Career Research Program Award, DE-SC0022988. The authors would like to thank the entirety of the University of Michigan Plasmadynamics and Electric Propulsion Laboratory (PEPL), in particular Dr. Tate M. Gill, Parker J. Roberts, and Declan G. Brick, for their assistance, advice, and helpful discussion throughout this effort. The authors would additionally like to thank Margaret M. Mooney from the Aerospace Laboratory for Plasma Experiments (ALPE) at Western Michigan University for helpful discussion on probe setup and design.

IX. Appendix

To infer linear growth rate, dispersion, and non-linear wave-wave-coupling from measured plasma density oscillations, we may start by assuming that our wave dynamics can be modeled by the following nonlinear wave coupling equation,

$$\frac{\partial \phi(k,t)}{\partial t} = (\gamma_k + i\bar{\omega}_k)\phi(k,t) + \frac{1}{2}\sum_{k=k_1+k_2} \Lambda_k^Q(k_1 k_2)\phi(k_1,t)\phi(k_2,t), \tag{14}$$

as proposed by Ritz et.al. Here γ_k and ω_k represents the imaginary and real parts of the dispersion relation corresponding to the growth rate and frequency of a wave with wave number k. $\Lambda_k^Q(k_1,k_2)$ is a function which describes the degree to which energy is coupled to a wave with wave number k by two other waves with wave numbers k_1 and k_2 where $k = k_1 + k_2$. Intuition for how two waves can couple energy to a third wave can be gained by drawing a parallel to acoustics where playing two notes simultaneously with similar frequencies results in an audibly distinguishable "beat" pattern at a third frequency. The domain of this nonlinear wave-wave coupling function encompasses all combinations of two wave numbers and the outputs are coefficients corresponding to the degree of wave-wave coupling of the wave pair to a third wave. The spatial Fourier spectrum $\phi(x,t)$ of the fluctuating density is defined by:

$$\phi(x,t) = \sum_k \phi(k,t)e^{ikx}. \tag{15}$$

In lay terms, we posit that the measured signal can be represented by a"weighted sum" of periodic functions where each function ($e^{ikx} = cos(kx)+isin(kx)$) encodes a particular wave with unique wavenumber k (spatial frequency). The weight ($\phi(k,t)$) assigned to each function is simply the amplitude corresponding to that wave. At a particular instance $t = t_o$, the measured signal can be described with a linear combination of waves (Fourier series) with coefficients given by $\phi(k,t_o)$. This set of Fourier coefficients is not static. It will change with time due to the propagation of the waves, i.e. the amplitudes of the waves will change through linear growth processes as well as nonlinear wave-wave interactions. It is therefore appropriate to represent this set of Fourier coefficients by a set of amplitudes and corresponding phases, where the amplitudes vary in time with respect to phase changes of the waves they describe.

$$\phi(k,t) = |\phi(k,t)|e^{i\Theta(k,t)}. \tag{16}$$

The change in the Fourier coefficients, or spectrum, can therefore be written as:

$$\frac{\partial \phi(k,t)}{\partial t} = \frac{\partial(|\phi(k,t)|e^{i\Theta(k,t)})}{\partial t}. \tag{17}$$

We note here the left hand side of equation 16 is the same as the left hand side of equation 14, our governing equation. Leveraging product rule, power rule, and chain rule, the right hand side of equation 17 can be expanded to:

$$\frac{\partial \phi(k,t)}{\partial t} = |\phi'(k,t)|e^{i\Theta(k,t)} + |\phi(k,t)| \cdot i\Theta'(k,t)e^{i\Theta(k,t)}. \tag{18}$$

We may then represent $|\phi'(k,t)|$ and $i\Theta'(k,t)$ using finite difference approximations where:

$$\begin{cases} |\phi'(k,t)| & = \frac{|\phi(k,t+\Delta t)|-|\phi(k,t)|}{\Delta t} \\ i\Theta'(k,t) & = \frac{i[\Theta(k,t+\Delta t)-\Theta(k,t)]}{\Delta t} \end{cases} \tag{19}$$

Substituting the above expressions into the equation 18 yields:

$$\frac{\partial \phi(k,t)}{\partial t} = \frac{1}{\Delta t}|\phi(k,t+\Delta t) - \phi(k,t)|e^{i\Theta(k,t)} + |\phi(k,t)| \cdot i\frac{1}{\Delta t}[\Theta(k,t+\Delta t) - \Theta(k,t)]e^{i\Theta(k,t)}. \tag{20}$$

We now set the right hand side of this equation equal to the right hand side of the governing equation (14):

$$\begin{aligned} &\frac{1}{\Delta t}|\phi(k,t+\Delta t) - \phi(k,t)|e^{i\Theta(k,t)} + |\phi(k,t)| \cdot i\frac{1}{\Delta t}[\Theta(k,t+\Delta t) - \Theta(k,t)]e^{i\Theta(k,t)} \\ &= (\gamma_k + i\bar{\omega}_k)\phi(k,t) + \frac{1}{2}\sum_{k=k_1+k_2} \Lambda_k^Q(k_1 k_2)\phi(k_1,t)\phi(k_2,t) \end{aligned} \tag{21}$$

Dividing both sides by $e^{i\Theta(k,t)}$ yields:

$$\begin{aligned}&\frac{1}{\Delta t}|\phi(k,t+\Delta t)|-|\phi(k,t)|+|\phi(k,t)|\cdot i\frac{1}{\Delta t}[\Theta(k,t+\Delta t)-\Theta(k,t)]\\&=\frac{\gamma_k+i\bar{\omega}_k}{e^{i\Theta(k,t)}}\phi(k,t)+\frac{1}{2}\sum_{k=k_1+k_2}\frac{\Lambda_k^Q(k_1k_2)}{e^{i\Theta(k,t)}}\phi(k_1,t)\phi(k_2,t)\end{aligned}\tag{22}$$

We now isolate $|\phi(k,t+\Delta t)|$ on the left hand side by moving all other terms to the right hand side:

$$\begin{aligned}&|\phi(k,t+\Delta t)|=\Delta t(\frac{\gamma_k+i\bar{\omega}_k}{e^{i\Theta(k,t)}}\phi(k,t)-|\phi(k,t)|\cdot i[\Theta(k,t+\Delta t)-\\&\Theta(k,t)]+|\phi(k,t)|+\frac{1}{2}\sum_{k=k_1+k_2}\frac{\Lambda_k^Q(k_1k_2)}{e^{i\Theta(k,t)}}\phi(k_1,t)\phi(k_2,t))\end{aligned}\tag{23}$$

Noting our previous definition of the spectrum in equation 16, we note the following rearrangements are equivalent:

$$\begin{cases}\phi(k,t)=|\phi(k,t)|e^{i\Theta(k,t)}\Rightarrow|\phi(k,t)|=\frac{\phi(k,t)}{e^{i\Theta(k,t)}}\\\phi(k,t+\Delta t)=|\phi(k,t+\Delta t)|e^{i\Theta(k,t+\Delta t)}\Rightarrow|\phi(k,t+\Delta t)|=\frac{\phi(k,t+\Delta t)}{e^{i\Theta(k,t+\Delta t)}}\end{cases}\tag{24}$$

Noting this equivalence, equation 23 can be recast as:

$$\frac{\phi(k,t+\Delta t)}{e^{i\Theta(k,t+\Delta t)}}=\Delta t(\frac{\gamma_k+i\bar{\omega}_k}{e^{i\Theta(k,t)}}\phi(k,t)-\frac{\phi(k,t)}{e^{i\Theta(k,t)}}\cdot i[\Theta(k,t+\Delta t)-\Theta(k,t)]+\frac{\phi(k,t)}{e^{i\Theta(k,t)}}+\frac{1}{2}\sum_{k=k_1+k_2}\frac{\Lambda_k^Q(k_1k_2)}{e^{i\Theta(k,t)}}\phi(k_1,t)\phi(k_2,t))\tag{25}$$

Noting the shared denominator of $e^{i\Theta(k,t)}$ in the first three terms on the left hand side, we may combine them into one term:

$$\frac{\phi(k,t+\Delta t)}{e^{i\Theta(k,t+\Delta t)}}=\Delta t(\frac{(\gamma_k+i\bar{\omega}_k)-i[\Theta(k,t+\Delta t)-\Theta(k,t)]+1}{e^{i\Theta(k,t)}}\phi(k,t)+\frac{1}{2}\sum_{k=k_1+k_2}\frac{\Lambda_k^Q(k_1k_2)}{e^{i\Theta(k,t)}}\phi(k_1,t)\phi(k_2,t))\tag{26}$$

As an aside, we note here that the factor of $\frac{1}{2}$ in front of the summation stems from the fact that $k=k_1+k_2$ allows for a "double counting" of the wave number pairs, i.e. every pair has a mirror case $k=k_2+k_1$ that gets factored into the summation. The factor of $\frac{1}{2}$ thus serves to correct this double counting. However, if we restrict the condition of the summation by imposing $k=k_1+k_2$ where $k_1>=k_2$ we, in effect, limit double counting and therefore equation 26 can be simplified slightly to:

$$\frac{\phi(k,t+\Delta t)}{e^{i\Theta(k,t+\Delta t)}}=\Delta t(\frac{(\gamma_k+i\bar{\omega}_k)-i[\Theta(k,t+\Delta t)-\Theta(k,t)]+1}{e^{i\Theta(k,t)}}\phi(k,t)+\sum_{\substack{k_1\geq k_2\\k=k_1+k_2}}\frac{\Lambda_k^Q(k_1k_2)}{e^{i\Theta(k,t)}}\phi(k_1,t)\phi(k_2,t))\tag{27}$$

(Kim et.al. used this double-count-corrected form for the summation in their paper.) Next, we multiply the entire equation by the denominator of the left hand side. Noting additionally that $e^x=\frac{1}{e^{-x}}$, we may lump this term into the denominator of the right hand side:

$$\phi(k,t+\Delta t)=\Delta t(\frac{(\gamma_k+i\bar{\omega}_k)-i[\Theta(k,t+\Delta t)-\Theta(k,t)]+1}{e^{-i[\Theta(k,t+\Delta t)-\Theta(k,t)]}}\phi(k,t)+\sum_{\substack{k_1\geq k_2\\k=k_1+k_2}}\frac{\Lambda_k^Q(k_1k_2)}{e^{-i[\Theta(k,t+\Delta t)-\Theta(k,t)]}}\phi(k_1,t)\phi(k_2,t))\tag{28}$$

As a last step, we define the following:

$$\begin{cases} Y_k = \phi(k, t+\Delta t) \\ X_k = \phi(k,t) \\ L_k = \Delta t(\frac{(\gamma_k + i\bar{\omega}_k) - i[\Theta(k,t+\Delta t) - \Theta(k,t)] + 1}{e^{-i[\Theta(k,t+\Delta t) - \Theta(k,t)]}} \\ Q_k^{1,2} = \Delta t(\frac{\Lambda_k^Q(k_1 k_2)}{e^{-i[\Theta(k,t+\Delta t) - \Theta(k,t)]}}) \end{cases} \tag{29}$$

Here we are simply choosing shorthand forms to recast the spectra at time $t + \Delta t$ as Y_k, the spectra at time t as X_k, the term encoding the linear growth and frequency as L_k and the nonlinear wave-wave coupling term as Q_k. Using these substitutions, we finally arrive at a compact form of our model for wave dynamics:

$$Y_k = L_k X_k + \sum_{\substack{k_1 \geq k_2 \\ k = k_1 + k_2}} Q_k^{1,2} X_{k_1} X_{k_2} \tag{30}$$

In lay terms, the equation simply posits that the spectra at time t (X_k) changes through both linear growth processes (L_k) and non-linear wave-wave interaction (Q_k), and thus evolves during a finite time-step Δt into the spectra observed at time $t + \Delta t$ (Y_k).

Following the formulation given in Ritz et al., we neglect the non-linear growth term in this work. Equation 30 thus becomes

$$Y_k = L_k X_k. \tag{31}$$

It is evident from the above result that the dispersion and growth rate are now comparatively trivial to solve for. We first expand L_k into its full form per equation 29

$$Y_k = \Delta t(\frac{(\gamma_k + i\bar{\omega}_k) - i[\Theta(k,t+\Delta t) - \Theta(k,t)] + 1}{e^{-i[\Theta(k,t+\Delta t) - \Theta(k,t)]}} X_k). \tag{32}$$

Next we divide by X_k and multiply the left hand side by X_k^*

$$\frac{Y_k X_k^*}{X_k X_k^*} = \Delta t(\frac{(\gamma_k + i\bar{\omega}_k) - i[\Theta(k,t+\Delta t) - \Theta(k,t)] + 1}{e^{-i[\Theta(k,t+\Delta t) - \Theta(k,t)]}}). \tag{33}$$

Given we can approximate from the auto-power and cross-power spectrum $e^{-i[\Theta(k,t+\Delta t) - \Theta(k,t)]} \approx \frac{\langle Y_k X_k^* \rangle}{\langle X_k X_k^* \rangle}$, Fourier transforming with respect to time instead of space [17], we may solve for both the dispersion and growth rate as

$$\gamma_f = \mathcal{R}e\left(\frac{|\langle Y_f X_f^* \rangle|}{\langle X_f X_f^* \rangle} - 1 + \ln\left(\frac{\langle Y_f X_f^* \rangle}{|\langle Y_f X_f^* |\rangle}\right)\right)\frac{1}{\Delta \vec{x}} \cdot \vec{v}_g, \tag{34}$$

$$k_{f(\Delta \vec{x})} = \mathcal{I}m\left(\frac{|\langle Y_f X_f^* \rangle|}{\langle X_f X_f^* \rangle} - 1 + \ln\left(\frac{\langle Y_f X_f^* \rangle}{|\langle Y_f X_f^* |\rangle}\right)\right)\frac{1}{\Delta \vec{x}}. \tag{35}$$

References

[1] B. A. Jorns, I. G. Mikellides, and D. M. Goebel, "Ion acoustic turbulence in a 100-a lab6 hollow cathode," *Phys. Rev. E*, vol. 90, no. 6, Dec. 2014. DOI: 10.1103/PhysRevE.90.063106.

[2] S. E. Cusson, S. E. Cusson, B. Jorns, B. A. Jorns, A. D. Gallimore, and A. D. Gallimore, "Ion acoustic turbulence in the hollow cathode plume of a hall effect thruster," *2018 Joint Propulsion Conference*, 2018. DOI: 10.2514/6.2018-4509.

[3] I. G. Mikellides, I. G. Mikellides, I. G. Mikellides, and I. G. Mikellides, "Theoretical model of a hollow cathode insert plasma," *null*, 2004. DOI: 10.2514/6.2004-3817.

[4] I. G. Mikellides, I. G. Mikellides, I. Katz, *et al.*, "Hollow cathode theory and experiment. ii. a two-dimensional theoretical model of the emitter region," *Journal of Applied Physics*, 2005. DOI: 10.1063/1.2135409.

[5] I. G. Mikellides, I. G. Mikellides, I. Katz, *et al.*, "Evidence of nonclassical plasma transport in hollow cathodes for electric propulsion," *Journal of Applied Physics*, 2007. DOI: 10.1063/1.2710763.

[6] A. D. Gallimore, A. D. Gallimore, J. L. Rovey, J. L. Rovey, D. A. Herman, and D. A. Herman, "Erosion processes of the discharge cathode assembly of ring-cusp gridded ion thrusters," *37th AIAA Plasmadynamics and Lasers Conference*, 2006. DOI: 10.2514/6.2006-3558.

[7] V. J. Friedly, V. J. Friedly, P. J. Wilbur, and P. J. Wilbur, "High current hollow cathode phenomena," *21st International Electric Propulsion Conference*, 1990. DOI: 10.2514/6.1990-2587.

[8] J. E. Foster, J. E. Foster, M. J. Patterson, M. J. Patterson, and M. J. Patterson, "Downstream ion energy distributions in a hollow cathode ring cusp discharge," *Journal of Propulsion and Power*, 2005. DOI: 10.2514/1.4771.

[9] D. M. Goebel, D. M. Goebel, D. M. Goebel, *et al.*, "Energetic ion production and electrode erosion in hollow cathode discharges," *29th International Electric Propulsion Conference*, 2005. DOI: null.

[10] D. M. Goebel, D. M. Goebel, K. K. Jameson, *et al.*, "Potential fluctuations and energetic ion production in hollow cathode discharges," *Physics of Plasmas*, 2007. DOI: 10.1063/1.2784460.

[11] A. Sengupta, A. Sengupta, A. Sengupta, *et al.*, "Status of the extended life test of the deep space 1 flight spare ion engine after 30,000 hours of operation," *39th AIAA/ASME/SAE/ASEE Joint Propulsion Conference and Exhibit*, 2003. DOI: 10.2514/6.2003-4558.

[12] A. Sengupta, A. Sengupta, A. Sengupta, *et al.*, "An overview of the results from the 30,000 hr life test of deep space 1 flight spare ion engine," *40th AIAA/ASME/SAE/ASEE Joint Propulsion Conference and Exhibit*, 2004. DOI: 10.2514/6.2004-3608.

[13] J. E. Polk, J. Polk, J. Polk, *et al.*, "An overview of the results from an 8200 hour wear test of the nstar ion thruster," *35th Joint Propulsion Conference and Exhibit*, 1999. DOI: 10.2514/6.1999-2446.

[14] I. G. Mikellides, I. G. Mikellides, I. Katz, *et al.*, "Wear mechanisms in electron sources for ion propulsion, 2: Discharge hollow cathode," *Journal of Propulsion and Power*, 2008. DOI: 10.2514/1.33462.

[15] B. A. Jorns, C. Dodson, D. M. Goebel, and R. Wirz, "Propagation of ion acoustic wave energy in the plume of a high-current lab6 hollow cathode," *Phys. Rev. E*, vol. 96, no. 2, Aug. 2017. DOI: 10.1103/PhysRevE.96.023208.

[16] R. Z. Sagdeev, R. Z. Sagdeev, A. A. Galeev, *et al.*, "Nonlinear plasma theory," *null*, 1969. DOI: null.

[17] Z. A. Brown and B. A. Jorns, "Growth and saturation of the electron drift instability in a crossed field plasma," *Phys. Rev. Lett.*, vol. 130, no. 11, Mar. 2023. DOI: 10.1103/PhysRevLett.130.115101.

[18] R. C. Davidson, R. Davidson, N. A. Krall, and N. Krall, "Anomalous transport in high-temperature plasmas with applications to solenoidal fusion systems," *Nuclear Fusion*, 1977. DOI: 10.1088/0029-5515/17/6/017.

[19] V. Y. Bychenkov, V. Y. Bychenkov, V. P. Silin, V. P. Silin, S. A. Uryupin, and S. A. Uryupin, "Ion-acoustic turbulence and anomalous transport," *Physics Reports*, 1988. DOI: 10.1016/0370-1573(90)90122-i.

[20] T. H. Stix, "Waves in plasmas: Highlights from the past and present," *Physics of Fluids B: Plasma Physics*, vol. 2, no. 8, pp. 1729–1743, Aug. 1990, ISSN: 0899-8221. DOI: 10.1063/1.859444. eprint: https://pubs.aip.org/aip/pfb/article-pdf/2/8/1729/12324051/1729_1_online.pdf. [Online]. Available: https://doi.org/10.1063/1.859444.

[21] D. G. Swanson, D. G. Swanson, and D. G. Swanson, "Plasma waves (2nd edition)," *Plasma Physics and Controlled Fusion*, 2003. DOI: 10.1088/0741-3335/45/6/701.

[22] A. L. Ortega, B. A. Jorns, and I. G. Mikellides, "Hollow cathode simulations with a first-principles model of ion-acoustic anomalous resistivity," *Journal of Propulsion and Power*, vol. 34, no. 4, pp. 1026–1038, 2018. DOI: 10.2514/1.B36782.

[23] J. M. Beall, J. M. Beall, Y. C. Kim, Y. C. Kim, E. Powers, and E. J. Powers, "Estimation of wavenumber and frequency spectra using fixed probe pairs," *Journal of Applied Physics*, 1982. DOI: 10.1063/1.331279.

[24] M. Georgin, "Ionization instability of the hollow cathode plume," Ph.D. dissertation, University of Michigan, Ann-Arbor, 2020.

[25] M. M. Mooney and K. M. Lemmer, "The effect of probe separation distance on the analysis of plasma waves in a cathode plasma," *AIAA SCITECH 2024 Forum*, 2024. DOI: 10.2514/6.2024-0923.

[26] C. P. Ritz, C. P. Ritz, E. Powers, E. J. Powers, and E. J. Powers, "Estimation of nonlinear transfer functions for fully developed turbulence," *Physica D: Nonlinear Phenomena*, 1986. DOI: 10.1016/0167-2789(86)90036-9.

[27] C. P. Ritz, C. P. Ritz, E. Powers, E. J. Powers, R. D. Bengtson, and R. D. Bengtson, "Experimental measurement of three-wave coupling and energy cascading," *Physics of fluids. B, Plasma physics*, 1989. DOI: 10.1063/1.859082.

[28] J. S. Kim, J. S. Kim, R. Durst, *et al.*, "Technique for the experimental estimation of nonlinear energy transfer in fully developed turbulence," *Physics of Plasmas*, 1996. DOI: 10.1063/1.871572.

[29] R. R. Hofer, S. E. Cusson, R. B. Lobbia, and A. D. Gallimore, "The h9 magnetically shielded hall thruster," *35th International Electric Propulsion Conference*, 2017. DOI: null.

[30] S. E. Cusson, R. R. Hofer, R. B. Lobbia, B. A. Jorns, and A. D. Gallimore, "Peformance of the h9 magnetically shielded hall thruster," *35th International Electric Propulsion Conference*, 2017. DOI: null.

[31] A. Brown and B. Jorns, "Dispersion relation measurements of plasma modes in the near-field plume of a 9-kw magnetically shielded thruster iepc-2017-387," *null*, 2017. DOI: null.

[32] P. J. Roberts and B. Jorns, "Characterization of electron mach number in a hollow cathode with thomson scattering," *AIAA SCITECH 2023 Forum*, 2023. DOI: 10.2514/6.2023-0843.

[33] S. Bromley, C. Sosolik, and J. Marler, "Symmetric charge exchange for intermediate velocity noble gas projectiles," *Journal of Physics B: Atomic, Molecular and Optical Physics*, vol. 52, Nov. 2019. DOI: 10.1088/1361-6455/ab42d1.

[34] I. G. Mikellides, I. G. Mikellides, A. L. Ortega, *et al.*, "Dynamics of a hollow cathode discharge in the frequency range of 1-500 khz," *Plasma Sources Science and Technology*, 2020. DOI: 10.1088/1361-6595/ab69e4.